Journal of Solid State Chemistry 184 (2011) 2167–2177

Contents lists available at ScienceDirect

Journal of Solid State Chemistry

journal homepage: www.elsevier.com/locate/jssc

Structural behavior and thermoelectric properties of the brownmillerite system $Ca_2(Zn_xFe_{2-x})O_5$

Emily Asenath-Smith *, Scott T. Misture, Doreen D. Edwards

Alfred University, Kazuo Inamori School of Engineering, Materials Science and Engineering, 2 Pine Street, Alfred, NY 14802, USA

ARTICLE INFO

Article history:
Received 11 January 2011
Received in revised form
7 June 2011
Accepted 10 June 2011
Available online 21 June 2011

Keywords:
Structure modulation
Browmillerite
Seebeck coefficient
Thermal properties
Electrical conductivity
High-temperature X-ray diffraction

ABSTRACT

The $Ca_2(Zn_xFe_{2-x})O_5$ series was synthesized and characterized to determine the influence of zinc dopant on the brownmillerite structure for thermoelectric applications. All single-phase compounds exhibited *Pnma* symmetry at room temperature up to the solubility limit at $x=0.10$. High-temperature X-ray powder diffraction was used to show that the nature of the *Pnma–Imma*$(0\,0\,\gamma)s00$ transition in $Ca_2Fe_2O_5$ is modified by the presence of zinc. While the Zn-free composition transitions to an incommensurate phase, the Zn-containing phases transition instead to a commensurate phase, *Imma*$(0\,0\,\gamma)s00$ with $\gamma=1/2$. Both the Néel temperature and the onset temperature of the *Pnma–Imma*$(0\,0\,\gamma)s00$ phase transition decreased with increasing zinc concentration. Rietveld analysis of the *in situ* diffraction pattern for the $x=0$ sample at 1300 °C demonstrates that the structure contains statistically disordered chain orientations as described by space group *Imma*. Thermoelectric properties were analyzed in air from 100 to 800 °C. The positive Seebeck coefficient revealed hole-type conduction for all compositions. Doped samples exhibited electrical conductivities up to 3.4 S/cm and thermal conductivity of 1.5 W/mK. Transport analysis revealed thermally activated mobility consistent with polaron conduction behavior for all compositions.

1. Introduction

The mineral srebrodolskite, $Ca_2Fe_2O_5$, dicalcium ferrite, is well studied both for inherent structural features and diverse applications. From a functional standpoint, dicalcium ferrite has been studied as a mixed-conductor for applications to oxygen separation membranes [1] and for anode materials in Li-ion batteries [2], with limited application. Other applications such as photocatalysis [3], biodiesel production [4], and propylene combustion [5] have been investigated. Structural interest in $Ca_2Fe_2O_5$ derives from its position as the iron endmember of the brownmillerite compositional series $Ca_2Fe_xAl_{2-x}O_5$, a perovskite derivative with ordered oxygen vacancies along [1 0 1]. The oxygen deficiency in perovskites is described as $A_nB_nO_{3n-1}$, with the brownmillerite endmember corresponding to $n=2$ stoichiometry [6,7]. Ordering of the oxygen vacancies (1/6) changes the coordination of half of the *B*-site cations from octahedral (*B*) to tetrahedral (*B′*) such that alternating layers of tetrahedra and octahedra stack in [0 1 0] direction yielding a formula described as $A_2BB'O_5$.

As illustrated in Fig. 1, interlayer ordering of tetrahedra in the brownmillerite structure has two main outcomes: *Pnma* (number 62) with alternating right- and left-handed tetrahedral chains; and *I2mb* (number 46) containing singly oriented tetrahedral chains. Intralayer variations are associated with two additional brownmillerite analogs: *C2/c* and *Pcmb* [8]. Additionally, those structures with statistically disordered tetrahedral chains exist with *Imma* [9] (*Icmm*, number 74) [10] symmetry, also shown to be incommensurately modulated *Imma*$(0\,0\,\gamma)s00$ [11]. Some brownmillerite compounds may disorder at high temperature to a perovskite phase, a direct result of the disordering of oxygen vacancies, which causes all bond lengths to approach one average value [12]. The ambient equilibrium phase of brownmillerite compounds depends on composition in terms of tetrahedral layer separation and chain distortion [8]. For example, the brownmillerite structural namesake, Ca_2AlFeO_5, has *I2mb* symmetry [13], while dicalcium ferrite crystallizes in space group *Pnma* at standard conditions [14]. The *Imma* (*Imma*$(0\,0\,\gamma)s00$) polymorph is typically found at high temperatures, with the transformation occurring at ~675 °C (700 °C) [14] in dicalcium ferrite [11].

The different inherent bond lengths of corner-linked tetrahedra and octahedra in the brownmillerite phase impart structural Jahn–Teller distortions, with resulting lattice polarizations that favor polaronic charge transport over band (itinerant) conduction [15]. Iron (III) in brownmillerite dicalcium ferrite exists in the high-spin state in both four-and six-fold coordination [10], facilitating *super-exchange* interactions and concomitant antiferromagnetic properties. Electronic conduction in $Ca_2Fe_2O_5$ above room temperature in air occurs by holes (*p*-type) [1,16], similar to other ferrite systems [17–19],

* Corresponding author. Fax: +607 871 2354.
E-mail address: easenath@mtholyoke.edu (E. Asenath-Smith).

0022-4596/$ - see front matter © 2011 Elsevier Inc. All rights reserved.
doi:10.1016/j.jssc.2011.06.009

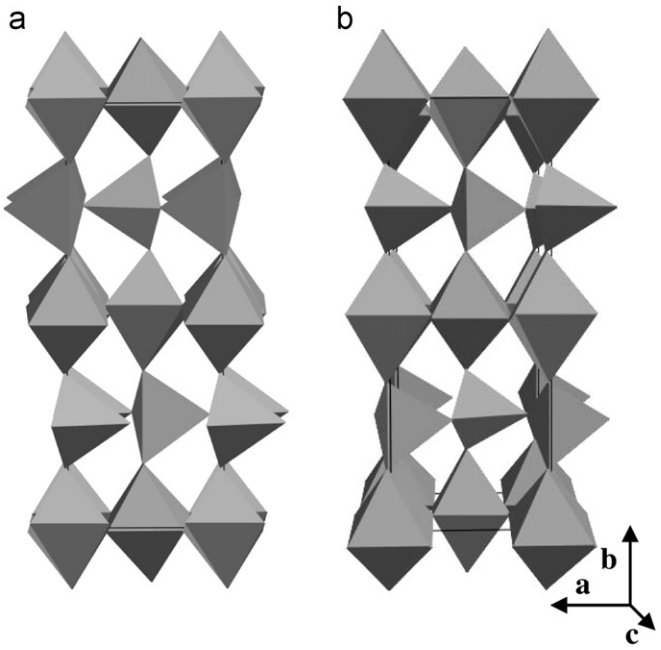

Fig. 1. Interlayer tetrahedral chain ordering in brownmillerite structures: (a) *Pnma* with alternating right-and left-handed tetrahedral chains and (b) *I2mb* with singly oriented tetrahedral chains. Oxygen ions define the coordination polyhedra and were omitted for clarity. A-site cations have been removed for clarity.

consistent with Eq. (1):

$$\frac{1}{2}O_2(g)+V_i^x+\Leftrightarrow O_i''+2h^{\bullet} \quad (1)$$

The variable valences of iron allow hole carrier association with Fe(III) ions to form *small* polarons (Fe^{4+} ions) [20] and Fe^{3+}—O^{2-}—Fe^{4+} networks along which electronic transport occurs in ferrite systems [17]. In dicalcium ferrite, ionic conductivity is low ($\sigma_i \sim 0.0007$ at 1000 °C), due to the two-dimensional nature of diffusion pathways, which limits oxygen vacancy movement to the $a-c$ plane [1].

B-site dopants in the dicalcium ferrite system have included Cu, Ni, Mg, and Zn [21], with many studies focused on magnetic properties. Other brownmillerite studies have looked at structural variations of the ambient phase with compositional changes [8], while only recently has the high temperature brownmillerite phase behavior in doped compositions been reported [10,22].

Site occupancy of *B*-site dopants (*B* vs. *B*′) in brownmillerite compounds can depend on crystal field effects and/or the relative sizes of the cations. For example, the crystal field stabilization energy associated with manganese (III) (d^4) ions favor its six-fold coordination [23,24]. Preferential four-fold coordination of Al (III) up to $x=2/3$ in $Ca_2Al_xFe_{2-x}O_5$ is attributed to its smaller size as compared to Fe (III) due to the absence of crystal field stabilization energy in both Al and Fe cations [10,25]. In the $Ca_2(Zn_xFe_{2-x})O_5$ system reported herein, high-spin iron (III) (d^5) shares similar electronic characteristics to zinc (II) (d^{10}): both exhibit zero crystal field stabilization energy in four- and six-fold coordination. In view of the tolerance factor, zinc (II) as a *B*-site ion would exhibit more distortion from the ideal cubic perovskite ($t=0.905$) than iron (III) ($t=0.945$), alluding to iron's preferential occupancy in the octahedral sites. However, when ionic size considerations are made, it is not obvious *a priori* that the larger zinc (II) ions will occupy the (smaller) tetrahedral (*B*′) sites in dicalcium ferrite.

Design of thermoelectric materials must conform to stringent thermal and electrical requirements as specified in the thermoelectric figure of merit (*ZT*), where $ZT=\alpha^2\sigma T_{avg}/\kappa$, α the thermopower (Seebeck coefficient), σ the electrical conductivity, and κ the total thermal conductivity. Oxide materials must achieve $ZT>1$ in order to be competitive. An expansion in the repertoire of *p*-type oxide thermoelectric materials serves to benefit from compatible pairing of *p*- and *n*-type oxide thermoelements in terms of their thermomechanical behavior [26,27] and similar temperature dependences in their Seebeck coefficients [28]. Herein the thermoelectric properties of the brownmillerite compound $Ca_2(Zn_xFe_{2-x})O_5$ are reported as prepared and analyzed in air for their application as a *p*-type thermoelectric material according to the following equation:

$$2ZnO+2CaO+\frac{1}{2}O_2(g)\xrightarrow{Ca_2Fe_2O_5}2Zn_{Fe}'+2h^{\bullet}+2Ca_{Ca}^{\times}+5O_o^{\times} \quad (2)$$

This particular brownmillerite system was chosen for the transition metal characteristics of iron, with zinc as an acceptor dopant to increase electrical conductivity and enhance thermal scattering by point defects. The goal of this study is two-fold: (i) to understand the effect of zinc dopant on the stability and phase behavior of dicalcium ferrite brownmillerite phases; and (ii) to expand the repertoire *p*-type thermoelectric oxides.

2. Experimental methods

Samples of $Ca_2(Zn_xFe_{2-x})O_5$, ($0 \le x \le 0.30$), were prepared using solid-state synthesis. Stoichiometric proportions of $CaCO_3$ (Alpha Aesar, 99.9%), Fe_2O_3 (Sigma-Aldrich, 99.9%), and ZnO (Sigma-Aldrich, ≥99.0%) were hand-mixed with isopropanol in an agate mortar and pestle. Powders were dried and sieved to ≤100 μm and ~2.0 g portions were pressed uniaxially to ~12 MPa using a Carver Model M die press. The pressed pellets were calcined in air at 900 °C (10 °C/min, 12 h), followed by reprocessing as above with reaction firing to 1000 °C. Product powders were ground and sieved as described above, with final mesh size of ≤30 μm. Sintered compacts were formed as described above with additional cold isostatic pressing to ~140 MPa. Samples were sintered to 1300 °C (10 °C/min, 12 h) in air. Densities were found using the Archimedes method (ASTM Standard C 373-88).

Product powders were analyzed by X-ray powder diffraction using Siemens θ-θ D5000 X-ray diffractometers equipped with Cu*K*α or Co*K*α radiation (40 kV, 30 mA) with three different experimental approaches: (i) room temperature phase identification measurements with scans from 10° to 90° 2θ (1°2θ/min) using Cu radiation; (ii) high temperature measurements taken during heating up to 1350 °C (20 °C/min) with scans taken every 25 °C using Co radiation to reduce the Fe fluorescence signal; and (iii) high temperature measurements taken during heating and cooling (T_{max}=1100 °C, 20 °C/min) with scans taken every 5 °C (1.5°2θ/min) over the range of 25–40°2θ using Cu radiation. The high-temperature *in situ* X-ray powder diffraction measurements were conducted on a customized diffractometer [29] with a Bruker Vantec position-sensitive detector and Pt-coated sapphire sample holder. Phase analysis was conducted using Jade 9 software (Materials Data Inc., USA). Unit cell dimensions and site occupancy were determined from Reitveld refinements using TOPAS software (Bruker AXS, Germany). Modulated structures were evaluated using the LeBail fitting option in JANA2006 [30]. Differential thermal analysis (DTA) was conducted in air from 100 to 1100 °C, with a heating and cooling rate of 20 °C/min, using an STA 449C TGA-DTA measurement system (NETZSCH Instruments, Germany). Sample sizes used were ~49, 43, and 48 mg for the x=0, 0.05, and 0.1 compositions, respectively.

Rietveld refinements of individual high-temperature X-ray powder diffraction patterns (every 100 °C) allowed the determination of lattice parameter temperature dependence according to Eq. (3). Standard error propagation was performed.

$$\alpha_L = \frac{1}{3}\alpha_v = \frac{1}{L_o}\left(\frac{dL}{dT}\right) \tag{3}$$

Microstructural images were taken with an Amray 1810 scanning electron microscope at 20 kV, using thermally etched (100 °C below sintering temperature, 1 h) fracture surfaces.

Sintered compacts were cut into $\sim 4 \times 4 \times 12$ mm bars for simultaneous electrical conductivity and Seebeck coefficient measurement based on the 4-point steady state gradient technique [31]. Sample bars were electroded with gold wire (Alfa Aesar, 99.9%) and conductive gold paste (Ted Pella, Inc, USA). Measurements were taken on a custom computer-controlled system with a current source (Model 2400 Keithley Instruments, Inc., USA), a digital multi-meter (Model 2700, Keithely Instruments, Inc., USA) and four type-R thermocouples (Pt/Pt-13%Rh). Thermal gradient was obtained by placing the sample off-center in a tube furnace, which allowed for ~ 10 °C temperature gradient along the length of the sample. Seebeck coefficient was found from linear regression of ΔV vs. ΔT plot made from the data of each individual measurement. The slope obtained was corrected for the platinum thermocouple leads according to $\alpha_{meas} = \alpha_{samp} + \alpha_{Pt}$. Reported thermopower values are the average of twenty complete measurements taken every 100 °C. Standard deviations were < 5 μV/K, with calculated error $< 10\%$ of reported values for $T < 300$ °C and $< 3\%$ for $T > 300$ °C. Direct current reversal was used to account for thermal electromotive force. Electrical conductivity values reported are the average of twenty measurements taken at each temperature, with standard deviations $< 1\%$ of the averages.

Thermal diffusivity (D_{th}) and specific heat (C_p), were found simultaneously using a Flashline 4010 laser-flash thermal diffusivity system (Anter Corporation, USA), Eq. (4):

$$\kappa = \rho C_p D_{th} \tag{4}$$

Thermal conductivity was calculated according to Eq. (4) along with bulk density (ρ).

3. Results

3.1. Phase stability and structural analysis

Brownmillerite phases of $Ca_2(Zn_xFe_{2-x})O_5$ ($x = 0.00$, 0.05, 0.10, 0.20, 0.30) were obtained by solid-state reactions conducted in air consistent with Kanamaru et al. [32], and confirmed to be orthorhombic *Pnma* (ICSD #00-018-0286). Room temperature X-ray powder diffraction patterns of the compositions studied, shown in Fig. 2a, illustrate the solubility limit of ZnO in $Ca_2Fe_2O_5$ by the emergence of additional peaks in the $x = 0.20$ samples. The peaks correspond to ZnO (Z), CaO (C) phases, with an additional unidentified phase(s) (U). Corresponding cell dimensions, shown in Fig. 2b, ceased to evolve after $x = 0.10$, confirming the limit of ZnO incorporation into the $Ca_2Fe_2O_5$ structure at $x = 0.10$. Only single-phase samples were used for further analyses.

Additional Rietveld analysis of the $x = 0.10$ X-ray powder diffraction pattern was used to confirm that the Zn-doped material has the same ambient crystal structure as the parent phase. By placing the Zn dopant on the tetrahedral Fe site, we achieved Rietveld statistics of $R_{wp} = 4.3\%$ and $R_p = 3.1\%$. Because the structure of the parent phase has been reported by several authors, we do not include the final refined structure for the Zn-doped material herein.

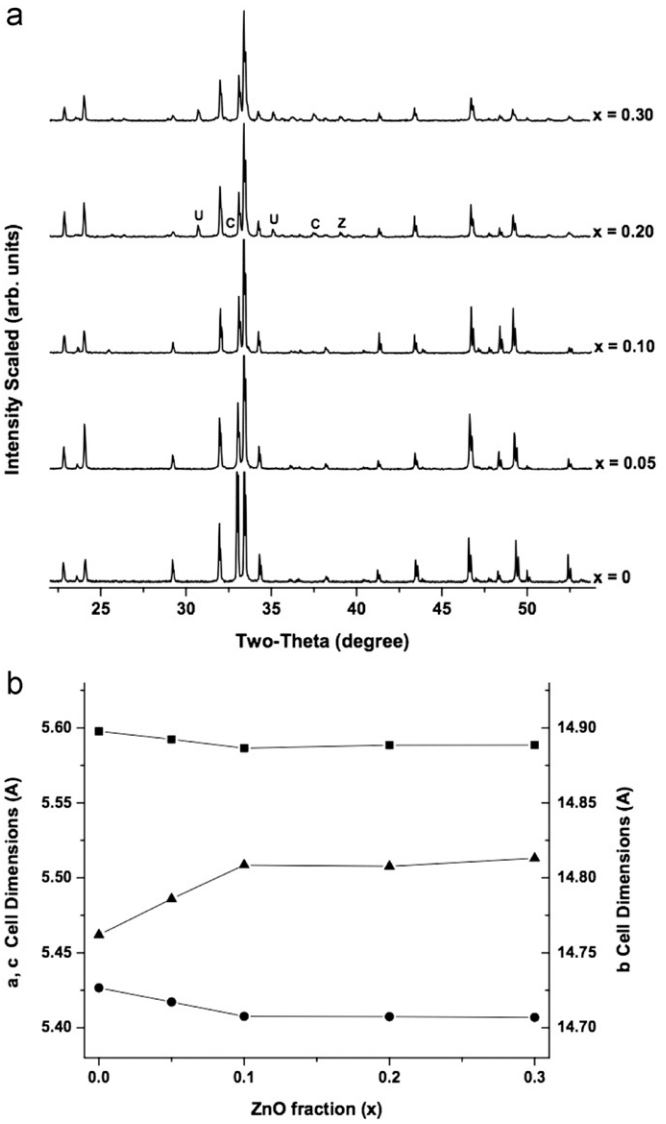

Fig. 2. (a) Room temperature X-ray powder diffraction patterns of $Ca_2(Zn_xFe_{2-x})O_5$ compositions illustrating the solubility limit at $x = 0.10$ by the emergence of additional phases at $x = 0.20$: Z=ZnO, C=CaO, and U=unidentified phase. (b) Evolution of cell dimensions: a (●), b (▲), c (■) with increasing dopant illustrating the solubility limit at $x = 0.10$. Error bars are smaller than data points and not shown.

3.2. In situ phase and structural analysis

3.2.1. Antiferromagnetic transition

Differential thermal analysis (DTA) was used to understand the stability range of products and monitor the Néel temperature, as shown in Fig. 3 and compiled in Table 1. An endotherm with onset at ~ 443 °C in the undoped $Ca_2Fe_2O_5$ sample confirmed the Néel temperature, with corresponding endotherms at 430 and 424 °C in the 0.05 and 0.10 compositions, respectively, exhibiting a linear decrease ($R^2 > 0.95$) with increasing zinc. On cooling, the reverse transition onset at $T_N = 445$, 390, and < 350 °C, in the $x = 0$, 0.05, 0.10 compositions respectively, illustrating a thermal hysteresis introduced by the zinc dopant (Table 1).

The decrease in the Néel temperature with increasing zinc is consistent with other reports in both oxide and non-oxide systems. For example, a decrease in T_N with increasing La-dopant was reported for the $CeIn_3$ system [33], and decreasing T_N with increasing x was reported in the $Ca_2Fe_{2-x}M_xO_{5-x/2}$ (M=Mg, Ni, Cu, Zn) system [21].

3.2.2. *Pnma–Imma(0 0 γ)s00 transition: phase characterization*

Although XRD measurements using Cu radiation showed some small satellite peaks from structure modulations, additional experiments using Co radiation were necessary to achieve acceptable signal-to-noise ratios for indexing the satellite peaks. Fig. 4a shows the *in situ* XRD data for the $x=0.1$ sample, wherein the *Pnma–Imma*(0 0 γ)s00 transition is obvious. Fig. 4b shows that the satellite peaks can be described using a *commensurate* modulation, with refined $\gamma=0.5009(2)$, and *Rwp*=5.2% and GOF=1.3. The commensurate modulation remains unchanged up to 1300 °C. We note the same result for the $x=0.05$ sample, with $\gamma=½$. In comparison, the Zn-free phase is well-known to take on an incommensurate modulation with $\sim0.58<\gamma<\sim0.62$, over the temperature range of 690–800 °C [11]. Therefore, we note that even small Zn additions lead to a preference for the superstructure to take on a periodic alternating right–left tetrahedral chain sequence. Commensurate modulations have been observed in similar systems, for example Sr_2MnGaO_5 [34]. The mechanisms responsible for chain ordering have been studied in some detail, with dipole–dipole interactions between tetrahedral chains being identified as a primary driving force for the various ordering sequences [35].

In addition, we have studied the $Ca_2Fe_2O_5$ material to higher temperatures than previous authors, and discovered additional phase transitions. Fig. 5 shows the *in situ* XRD data for $Ca_2Fe_2O_5$, demonstrating the *Pnma–Imma*(0 0 γ)s00 phase transition. As reported by Krüger et al. [11], the modulation vector changes with temperature, decreasing from 0.62 at 700 °C to 0.59 at 900 °C. Krüger and co-workers predicted that continued heating might result in a superstructure with alternating chains. Indeed we have observed this phase transition, which occurs on heating above 1000 °C. As shown in Fig. 5, a 2-phase mixture of modulated phases with $\gamma=0.59$ and ½ is found at 1000 °C, and then the modulation satellites decrease in intensity on approaching 1300 °C. At 1300 °C and higher, the peaks may be described using space group *Imma*, wherein there is statistical disorder among the L and R chains rather than the alternating –L–R–L–R– sequence characteristic of the commensurate structure. A Rietveld refinement of the 1300 °C XRD data was performed to confirm the *Imma* space group, though we note that a full refinement was not performed because of the limited angular range of the *in situ* dataset. As shown in Fig. 6 and Table 2, the *Imma* model accurately describes the $Ca_2Fe_2O_5$ structure at 1300°C.

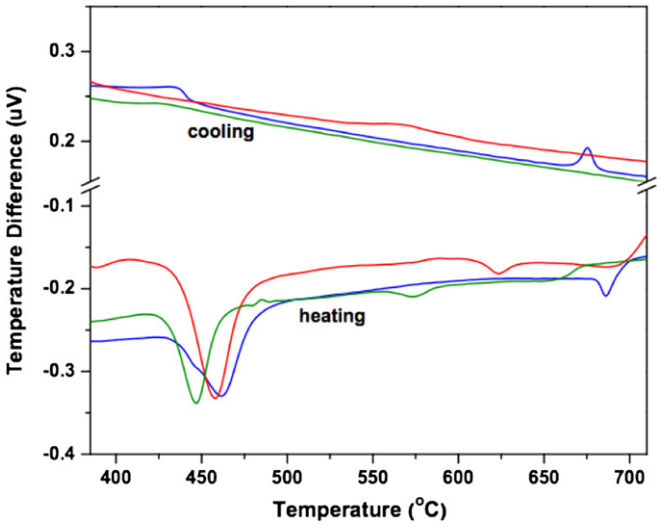

Fig. 3. Differential thermal analysis of $Ca_2(Zn_xFe_{2-x})O_5$ compositions showing $x=0$ (blue), $x=0.05$ (red), and $x=0.10$ (green). The Nèel transition is seen during heating in the endotherms centered around ~450 °C. The *Pnma–Imma*(0 0 γ)s00 phase transition is seen during heating as endotherms around 550–675 °C. During cooling the *Imma*(0 0 γ)s00–*Pnma* transitions are seen to become increasingly broadened with increasing zinc concentration.

3.2.3. *Pnma–Imma(0 0 γ)s00 transition: hysteresis*

High-temperature *in situ* X-ray powder diffraction (HTXRD) was used in conjunction with DTA to monitor the *Pnma–Imma*(0 0 γ)s00 transition of these brownmillerite compounds. Consistencies between DTA and HTXRD results included the decreasing onset temperatures for the forward *Pnma–Imma*(0 0 γ)s00 phase transition, manifest in the second endotherm (DTA) and the disappearance of (1 3 1) peaks at 29°2θ in a similar manner to that shown in Fig. 4 for the $x=0.1$ composition [10,36]. Upon cooling, *Pnma–Imma*(0 0 γ)s00 exotherms became increasingly broadened and onset at lower temperatures (690, 610, ~500 °C), indicating a thermal hysteresis introduced by the zinc dopant. The lack of hysteresis in the Zn-free sample is in disagreement with the recent report by Krüger et al. [11], who showed a hysteresis of ~24 °C during a DTA measurement with maximum temperature of 1000 °C. As described above, our DTA excursion to 1100 °C brought the sample into the range of the commensurately modulated phase emergence. We attribute the lack of hysteresis in the Zn-free sample to the added complexity of the additional phase transitions that occur at temperatures above 1000 °C. For the Zn-containing specimens, however, there is only a single transition, from *Pnma* to the commensurately modulated structure.

Kinetic information regarding the rate of the high-temperature phase transformation both upon heating and cooling was obtained from the number of diffraction peaks, taken every 5 °C, between the onset of decreased intensity in and complete disappearance of the (1 3 1) reflection. The results are compiled in Table 1. The temperature range over which the *Pnma–Imma*(0 0 γ)s00 phase transition occurred expanded from 10°C in the undoped dicalcium ferrite, to ~25 °C in the $x=0.10$ composition during heating. This result is in agreement with the work of Krüger and co-workers, who noted phase coexistence in

Table 1
Transition temperatures of thermal events in $Ca_2(Zn_xFe_{2-x})O_5$ found by DTA *in situ* high temperature X-ray powder diffraction.[a]

x	DTA (±1 °C)				XRD (±5 °C)				
	Neel temp.	*Imma*(0 0 γ)s00 onset temp. (heating)	*Pnma* onset temp. (cooling)	Phase transition hysteresis	*Imma*(0 0 γ)s00 Onset temp. (heating)	$\Delta T_{heating}$ transition range	*Pnma* Onset temp. (cooling)	$\Delta T_{cooling}$ transition range	Phase transition hysteresis
0.00	443	682	680	<2	690	10	690	10	<5
0.05	430	613	605	8	615	15	610	20	5
0.10	424	561	~500	~40	555	~25	~575	~40	n/a

[a] Temperatures indicated as approximate result from broadened peaks (DTA, Fig. 2, and HTXRD, Fig. 4c).

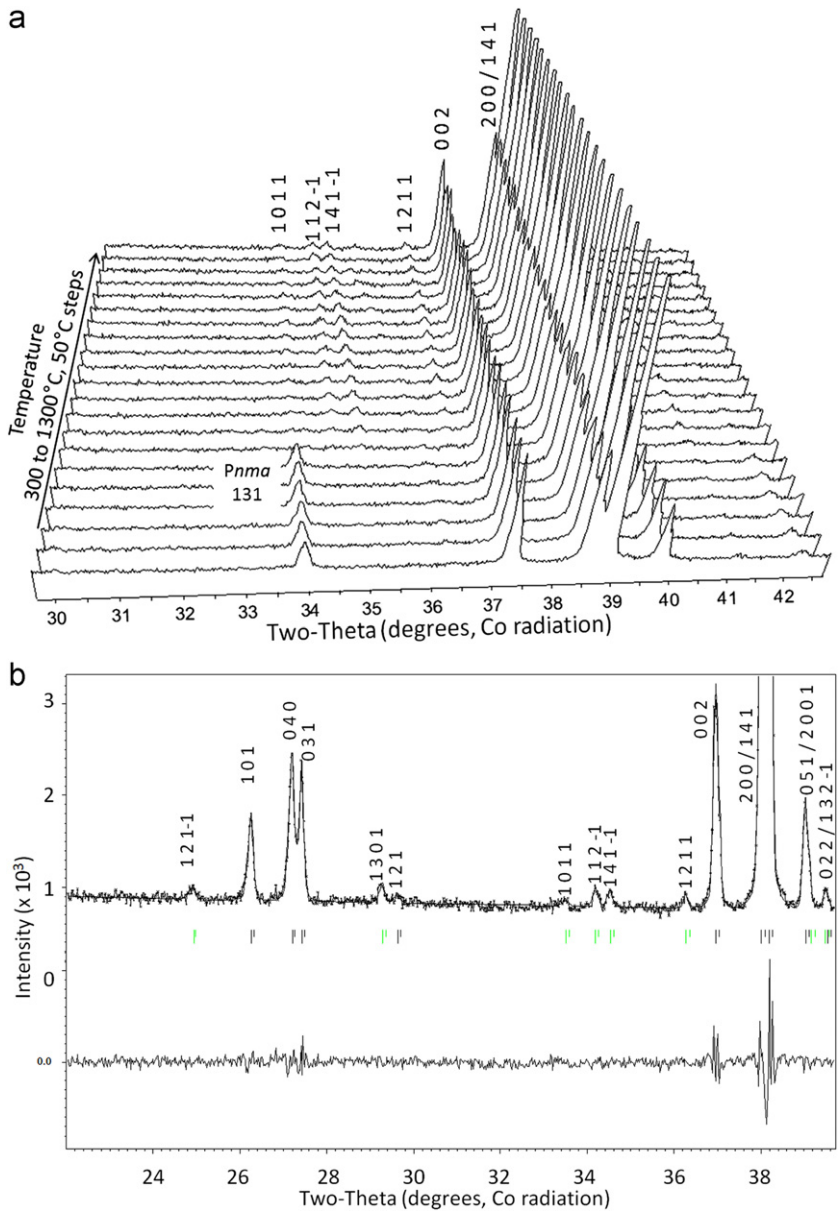

Fig. 4. *In situ* XRD data for the $x=0.1$ sample. (a) 3-D view of the full temperature range; (b) LeBail fit of the *in situ* X-ray powder diffraction pattern of the $x=0.1$ sample at 1250°C, using space group *Pnma–Imma*$(0\ 0\ \gamma)s00$ with refined $\gamma=0.5009(2)$.

$Ca_2Fe_2O_5$ during the *Pnma–Imma*$(0\ 0\ \gamma)s00$ transition. We note a similar situation in the case of the incommensurate to commensurate transition in the Zn-free sample, where the transition is extremely sluggish, with the peaks coexisting for at least 50 °C. Upon cooling, the reemergence of the (1 3 1) peaks onset at lower temperatures, again showing thermal hystereses that increased with increasing dopant. In the $x=0.10$ composition the prevalence of modulation reflections [11,37] at high temperature obscured the distinct reemergence of the (1 3 1) peak regardless of radiation source, yielding a hysteresis that could not be accurately quantified.

3.2.4. Thermal expansion

The temperature evolution of lattice parameters (normalized) shown in Fig. 7 for the $x=0.10$ composition is representative of all single-phase samples and illustrates predominate thermal expansion in [0 1 0]. Linear coefficients of thermal expansion were calculated separately for each cell direction of each phase and compiled in Table 3 [10,36].

3.3. Microstructural characterization

Only single-phase compositions were formed into sintered compacts and used for thermoelectric analyses, with representative microstructures shown in Fig. 8a–c. Measured densities were 3.70, 3.64, 3.71 g/cm^3 for the compositions $x=0$, 0.05, 0.10, respectively. Theoretical densities of 4.026, 4.028, 4.051 g/cm^3, respectively, were calculated using refined lattice parameters. Consistent with sintered densities $>90\%$ theoretical, all microstructures show evidence of the final stages of sintering, as evidenced by intragranular pores. Additionally, increasing grain size is observed with increasing dopant levels pointing toward the ability of zinc to enhance grain growth.

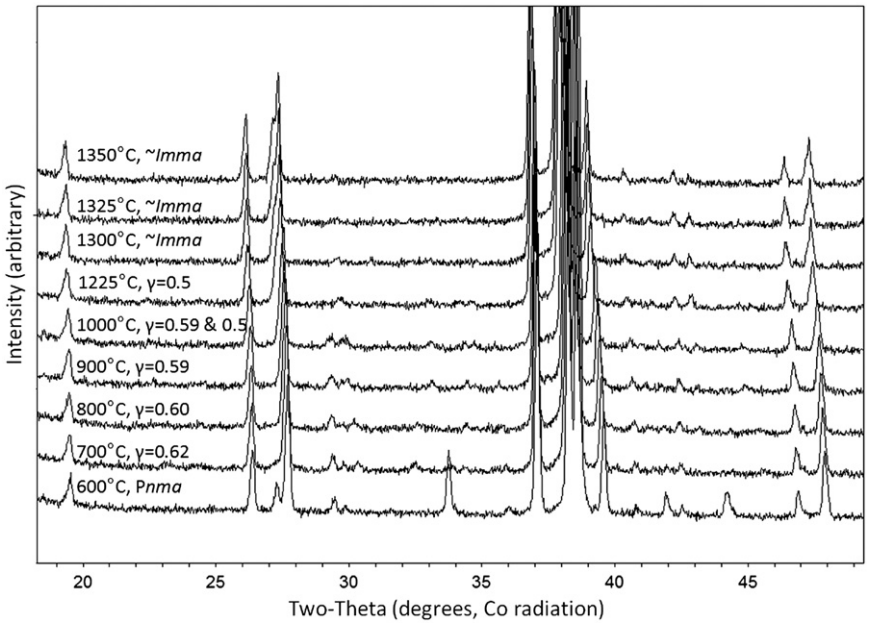

Fig. 5. *In situ* XRD data for the $x=0$ sample, from 600 to 1350°C. The progression of the modulation vector is indicated. Two values of γ indicates a 2-phase mixture with both modulations.

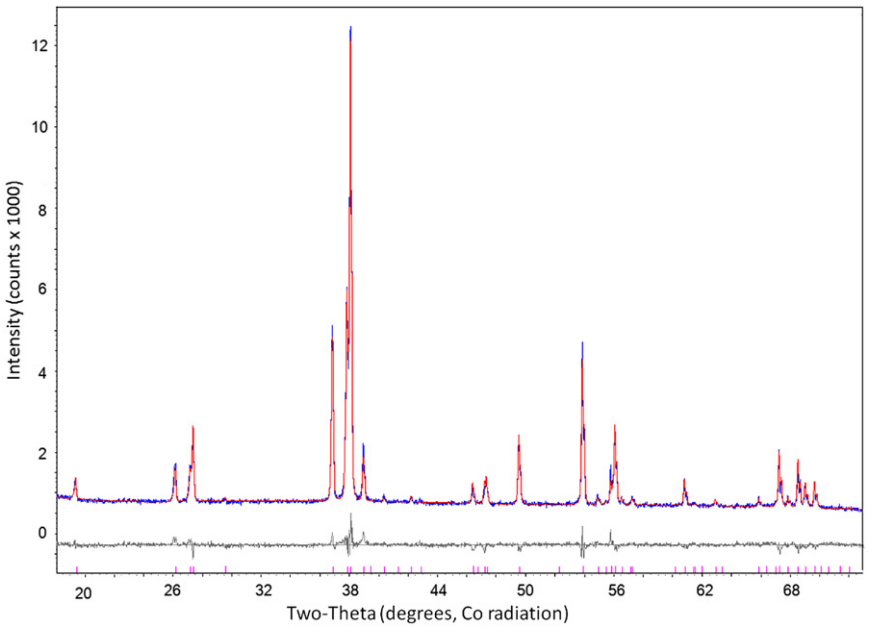

Fig. 6. Rietveld fit to the *in situ* X-ray powder diffraction pattern for the $x=0$ sample at 1300 °C showing correspondence with the *Imma* phase.

3.4. Thermoelectric properties

3.4.1. Seebeck coefficient and electrical conductivity

Direct current electrical conductivity (σ) and Seebeck coefficient (thermopower, α) were measured simultaneously from 100 to 800 °C, as shown in Fig. 9a,b, respectively. Electrical conductivity increased with temperature in all compositions, while only the $x=0.10$ samples exceeded 1 S/cm above 400 °C. Seebeck coefficients were positive over all temperatures indicating conduction by hole carriers. While Seebeck coefficient decreased with increasing temperature above 300 °C in the $x=0$ composition, the doped samples appear to approach a constant value over the same temperature range.

3.4.2. Thermal conductivity

Thermal conductivity results for all three compositions are shown in Fig. 9c. While a small decrease in thermal conductivity was seen with increasing dopant, all samples remained >1 W/mK.

3.5. Conduction analysis

Based on introductory remarks and previous calculations of $Ca_2Fe_2O_5$ [16], the $Ca_2(Zn_xFe_{2-x})O_5$ conduction behavior was analyzed according to a polaron model. The hole-type conduction in dicalcium ferrite was explained by the presence of oxygen interstitials consistent with Eq. (1), where hole carriers associated

Table 2
Structural refinement results for $Ca_2Fe_2O_5$, confirming the existence of *Imma* ($Fe_8Ca_8O_{20}$) phase at 1300 °C.[a, b]

Atom	Site	Multiplicity	Wyckoff position	x	y	z	Occ.
Ca^{2+}	Ca1	8	8 *h*	0(0)	0.1114(2)	0.5277(6)	1
Fe^{3+}	Fe1	4	4 *a*	0(0)	0(0)	0	1
Fe^{3+}	Fe2	8	8 *i*	0.058(1)	0.25(0)	0.0674(8)	0.5
O^{2-}	O1	8	8 *g*	−0.25	0.0049	0.25	1
O^{2-}	O2	16	16 *j*	−0.0123	0.1457	-0.041	0.5
O^{2-}	O3	8	8 *i*	−0.8897	0.25	0.3751	0.5

[a] R_{wp}=5.9%, GOF=1.8, *Imma*: a=5.5132(1) Å, b=15.2150(4) Å, c=5.6540(2) Å.
[b] Refinements were conducted using the model of Wright et al.[56]. Due to limited 2θ range of data, only cation positions were refined. Entries without error values were not refined.

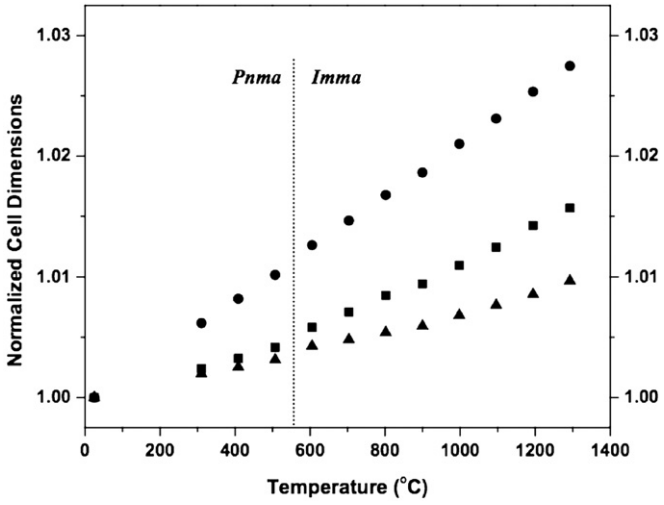

Fig. 7. Normalized cell dimensions of $Ca_2Zn_{0.10}Fe_{1.90}O_5$ product powders obtained from high temperature X-ray powder diffraction data: a (■), b (●), c (▲). Error bars are smaller than data points and are not shown.

Table 3
Linear coefficient of thermal expansion of single phase $Ca_2(Zn_xFe_{2-x})O_5$ compounds.

x	α_L ($\times 10^6$ K^{-1}) *Pnma*			α_L ($\times 10^6$ K^{-1}) *Imma*(0 0 γ)s00		
	a	*b*	*c*	*a*	*b*	*c*
0	9.8(3)	21.9(3)	8.1(3)	13.1(3)	23.3(4)	6.5(3)
0.05	9.4(3)	21.6(3)	7.4(3)	14.0(7)	22.0(7)	6.9(7)
0.10	8.6(3)	21.2(3)	6.5(3)	14.3(3)	21.4(3)	7.8(3)

with (variable valence) Fe cations, forming polarons as follows:

$$Ca_2Fe_2O_5 + \frac{1}{2}O_2(g) + V_i^{\times} \rightarrow 2Ca_{Ca}^{\times} + 2(Fe^{3+} + h^{\bullet}) + O_i'' + 5O_o^{\times} \quad (5)$$

Essentially, the conduction mechanism depends on the nature of the mobility, which can be distinguished through analysis of electrical conductivity and Seebeck coefficient as shown in Eqs. (6) and (7), respectively:

$$\sigma T = \sigma_o \ \exp\left(\frac{E_\sigma}{k_B T}\right) \quad (6)$$

$$\alpha = \frac{S}{e} = \frac{Q}{eT} = \frac{k_B}{e}\left(\frac{E_\alpha}{k_B T} + A\right) \quad (7)$$

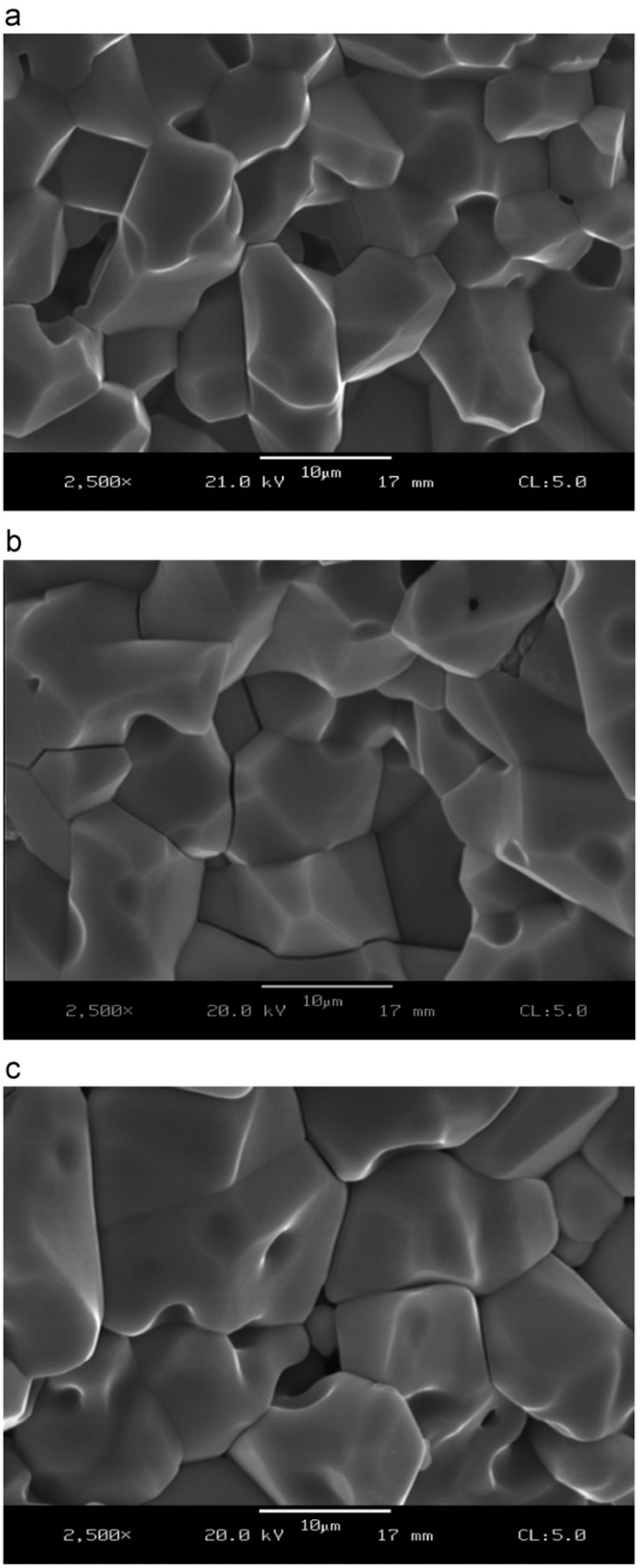

Fig. 8. Representative microstructures of single phase sintered compacts, $Ca_2(Zn_xFe_{2-x})O_5$, used for thermoelectrical measurements: (a) x=0, (b) x=0.05, (c) x=0.10.

Eq. (6) applies to the characteristic diffusion-like transport of polaron conduction, which results in a temperature-activated mobility. In this expression, (E_σ) represents the activation energy for

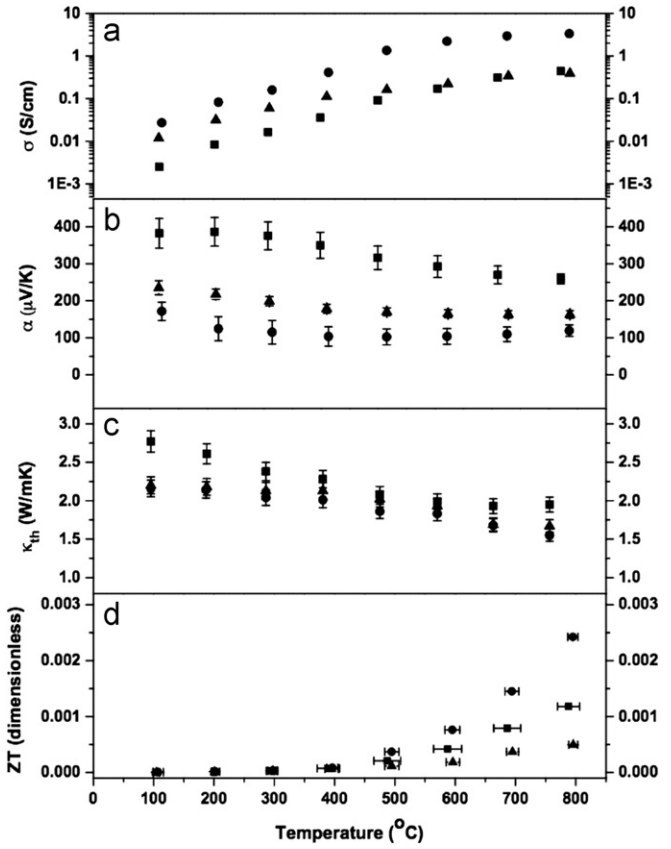

Fig. 9. Thermoelectric properties of $Ca_2(Zn_xFe_{2-x})O_5$: (a) direct current electrical conductivity (σ) (error bars are smaller than series symbols and not shown); (b) Seebeck coefficient (α); (c) thermal conductivity (κ_{th}); and (d) figure of merit (ZT). $x=0$ (■), $x=0.05$ (▲), $x=0.10$ (●).

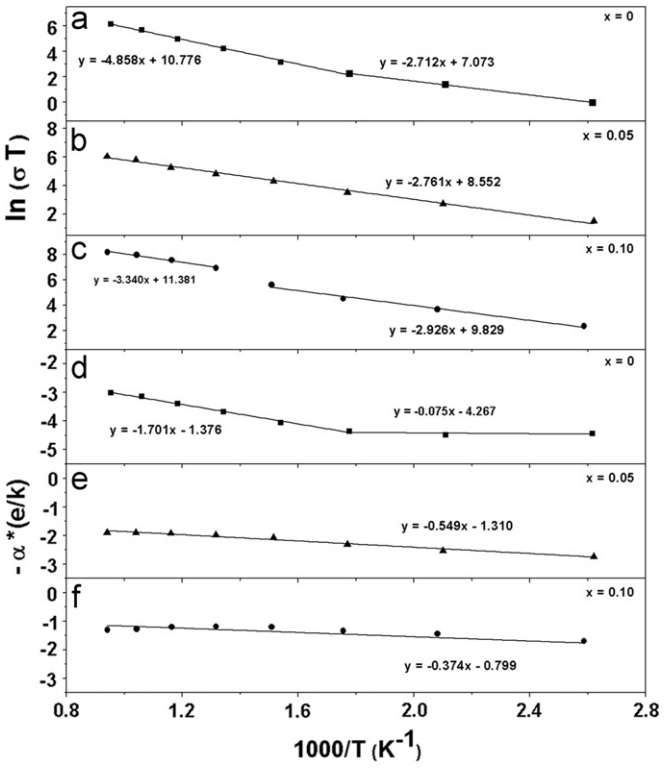

Fig. 10. Transport analysis of electrical conductivity (sigma) (a)–(c) and Seebeck coefficient (alpha) (d)–(f) data.

conduction, which contains contributions from both carrier generation (E_α) and the polaron binding energy (W); σ is the electrical conductivity; T the absolute temperature; k_B Boltzmann's constant; and σ_o includes geometrical and frequency factors. Eq. (7) results from the application of the second law of thermodynamics to thermopower, where S is the entropy, the heat of electronic conduction Q is related to the carrier generation energy (E_α), e is the electron elementary charge, and A represents the entropy of transport [38,39].

Arrhenius plots of conductivity (Eq. (6)) and thermopower (Eq. (7)) data shown in Fig. 10 were used to extract the corresponding activation energies (compiled in Table 4) and distinguish the charge transport mechanism. The $x=0$ composition shows two distinct regions of conduction behavior. The temperature at which the conductivity behavior changes, 300 °C, in the $x=0$ samples does not correspond to T_N or the temperature of the *Pnma–Imma*(0 0 γ)*s*00 transition. The discontinuity seen in the electrical conductivity data of the $x=0.10$ samples near T_N manifests in the corresponding Arrhenius plot (Fig. 10c) and two separate linear fits were used above and below the discontinuity to yield two regions with similar slopes and thus similar activation energies, thereby representing a single conduction mechanism.

Table 4
Activation energies derived from electrical conductivity[a] and Seebeck coefficient.[b]

Activation energy	$x=0$ (eV)		$x=0.05$ (eV)	$x=0.10$ (eV)
	$T<300$ °C	$T>300$ °C		
E_σ	0.23	0.42	0.23	0.25, 0.29
E_α	0.01	0.15	0.05	0.03
$E_\sigma - E_\alpha$	0.22	0.27	0.18	0.22, 0.26

[a] Activation energy for conduction (E_σ) contains both carrier generation and mobility contributions.
[b] Activation energy for carrier generation (E_α) derived from Seebeck coefficient measurements.

4. Discussion

4.1. Phase stability and structural analysis

4.1.1. Solubility limit and site occupancy

The limit for zinc incorporation in dicalcium ferrite at $x=0.10$ (5%) is consistent with other reports [21], while the evolution of lattice parameters with doping provided insight about the site occupancy of zinc ions. With continuous corner-shared polyhedra in [0 1 0] as well as within the octahedral sheets (*a–c* plane), as illustrated in Fig. 1, substitution of a larger ion into an octahedral site should mandate an expansion of the lattice in all directions. However, given the absence of corner sharing within tetrahedral sheets, substitution of a larger ion at a tetrahedral site can only strictly require expansion along [0 1 0]. The simultaneous contraction in *a–c* and expansion in the *b*-dimensions of the *Pnma* cell with zinc doping (Fig. 2b) provided evidence for zinc's preferential occupancy at tetrahedral sites. These findings show consistency with the $Ca(Al_xFe_{2-x})O_5$ compositional series, where aluminum ions occupy tetrahedral sites up to 2/3 [10].

4.1.2. Pnma–Imma(0 0 γ)s00 phase transition

Tetrahedral site occupancy of zinc dopant ions in dicalcium ferrite had a multi-faceted impact on the *Pnma–Imma*(0 0 γ)*s*00 phase transition with increasing dopant. In addition to changing

the high temperature polymorph to a commensurately modulated structure, Zn addition also decreased the onset temperature of the *Pnma–Imma*(0 0 γ)*s*00 phase transition and the rate of this phase transition, as manifest in the larger temperature ranges. Further, zinc introduced a thermal hysteresis between the forward and reverse phase transition that increased with increasing dopant. These results are consistent with the preferential substitution of zinc at tetrahedral sites and the central role that tetrahedral sites play in the *Pnma–Imma*(0 0 γ)*s*00 phase transition.

4.1.3. Linear coefficient of thermal expansion

All single-phase compositions exhibited anisotropic thermal expansion similar to that of the $x=0.10$ composition shown in Fig. 7. Consistent with brownmillerite polyhedral linkages and the zinc occupancy, these compounds exhibit the greatest expansion in [0 1 0], as compared to the *a–c* plane. These observations are consistent with a structure that has available space to accommodate thermal vibrations as well as larger dopant ions within the tetrahedral layers. The presence of Zn-dopant in the dicalcium ferrite brownmillerite structure was seen to have different effects on the linear coefficients of thermal expansion (CTE) of the *Pnma* and *Imma*(0 0 γ)*s*00 phases, as shown in Table 3. A decrease in CTE with increasing dopant was observed in all directions of the *Pnma* phase, while the *Imma*(0 0 γ)*s*00 phase showed negligible decrease in the inherent anisotropy: increasing thermal expansion in the *a*- and *c*-directions combined with decreasing expansion in the *b*-direction. To translate these results to the bulk, linear thermal expansion coefficients were calculated based on Eq. (3) using cell volume expansion data. The values found of 13.3(2), 12.7(3), $12.1(2)\times10^{-6}\,K^{-1}$ for the *Pnma* phase of the $x=0$, 0.05, 0.10 compositions, respectively, show a small but significant decrease in thermal expansion with increasing dopant. The *Imma*(0 0 γ)*s*00 phase showed no significant change in CTE with increasing dopant, with values of 14.4(2), 14.5(3), $14.3(2)\times10^{-6}\,K^{-1}$. These values can be considered representative of the behavior of a bulk polycrystalline sample due to the independence of thermal expansion on microstructure and porosity [40].

4.2. Thermoelectric properties

4.2.1. Electrical conductivity

Electrical conductivity, shown in Fig. 9a, increased with zinc concentration, confirming zinc as an acceptor dopant to increase (hole) carrier concentration in accordance with Eq. (2). Although the $x=0$ and 0.05 samples approached 0.4 S/cm above 600 °C, the $x=0.10$ composition reached conductivities of 3.4 S/cm at 800 °C, remarkably high for a polycrystalline brownmillerite compound [1,22,41].

A discontinuity in the electrical conductivity of the 0.10 samples was noted to fall in the range of the Néel temperature of this sample (424 °C found by DSC, Table 1). A similar but more subtle discontinuity was seen in the 0.05 samples (T_N=430 °C), while the $x=0$ samples appeared to exhibit a smooth trend over the entire temperature range. The manifestation of the Néel transition in the electrical conductivity data has been previously reported [42–44]. While some researchers have noted discontinuities near or around T_N, others noted the discontinuity directly at T_N and used electrical conductivity measurements to directly determine the Néel temperature [42]. The extent to which this transition reveals itself in the electrical data may depend on the type of conduction mechanism present. Whall et al. [44] observed a distinct break in their electrical conductivity data at T_N in manganese ferrite and attributed it to an increase in the polaron hopping energy during the Néel transition.

4.2.2. Seebeck coefficient

As seen in Fig. 9b the Seebeck coefficient of all samples remained positive over all temperatures, confirming charge transport by hole carries. The observed decrease in the Seebeck coefficient with increasing dopant is consistent with an increasing carrier concentration and the inverse relationship between Seebeck coefficient and carrier concentration. In both doped samples, $x=0.05$, 0.10, the Seebeck coefficients were found to approach constant (temperature independent) values of 160 and 110 μV/K, respectively.

4.2.3. Thermal conductivity

As seen in Fig. 9c, the presence of zinc dopant served to decrease thermal conductivity by ~1 W/mK at 100 °C over undoped samples, consistent with the increased thermal scattering potential of the larger zinc ion. Minimum thermal conductivity of ~1.5 W/mK was found at 800 °C in the $x=0.10$ doped samples, and noted to approach the target value of $\kappa\leq1$ W/mK for thermoelectric oxides.

4.2.4. Figure of merit

The thermoelectric figure of merit (ZT) as a function of average temperature for single phase $Ca_2(Zn_xFe_{2-x})O_5$ compounds are shown in Fig. 9d. Consistent with power factors that remained $\leq5\times10^{-6}$ W/mK^2 and thermal conductivities >1 W/mK, the maximum ZT value observed was ~0.002 at 800 °C in the $x=0.10$ composition.

4.3. Transport behavior in $Ca_2(Zn_xFe_{2-x})O_5$ system

Understanding thermoelectric phenomenon starts with an analysis of the coupling between thermal and electrical transport according to non-equilibrium thermodynamics [45–47]. The result illustrates thermopower to represent the entropy per carrier (*S*/*e*) [48], with increased thermopower achieved by maximizing the spin orbital degeneracies in the electronic structure of constituent ions [49,50]. For a polaron conductor, the consequences are two-fold: carriers require energy activation to move, and their association with lattice sites supports the statistical nature of this diffusion-like transport. Accordingly, the carrier generation energy (E_α) is very small, and the conduction activation energy (E_σ) is dominated by the mobility. The statistical nature points towards modeling the thermopower by Boltzmann's equation [51,52]:

$$\alpha=\frac{S}{e}=\pm\left(\frac{k_B}{e}\right)\left[\ln\left(\beta\frac{1-c}{c}\right)+\frac{S_v}{k_B}\right] \tag{8}$$

In this expression, c represents the fractional number of carriers (i.e. tetravalent iron), and S_v is the vibrational (transport) entropy associated with the charge carriers. Often, S_v/k_B is neglected, as it is estimated to contribute only 10 μV/K [53]. The factor β represents the spin orbital degeneracy [51]:

$$\beta=\frac{2S_n+1}{2S_{n+1}+1} \tag{9}$$

where S_n is the spin value of the M^{n+} cation (Fe^{3+}) and S_{n+1} is the spin value of the M^{n+1} cation (Fe^{4+}). In the high-spin iron system described herein, $\beta=6/5$. Carrier concentration (p) can be derived from c in Eq. (8) to estimate the mobility using $\sigma=ep\mu_h$. The polaron mobility calculated in this way should be <0.01 cm^2/Vs.

The transport mechanism for hole carriers in doped dicalcium ferrite compositions was found using the activation energies for carrier generation (E_α) and conduction (E_σ). In the case of polaron conduction, $E_\sigma=E_\alpha+W$, where W is the polaron binding energy: the activation energy associated with the mobility [54]. Being that the thermoelectric effect exists (and is measured) in the absence

of a current ($i=0$), the carrier activation energy (E_α) contains no contribution from the mobility [38]. The negligible temperature dependence of the thermopower, as seen in Fig. 10(e and f), qualitatively illustrates the absence of a temperature-activated carrier generation (i.e. itinerant conduction behavior). Quantitatively, the low activation energies (E_α) at 0.05, 0.03 eV for the $x=0.05$, 0.10 compositions, respectively, support a diffusion-like transport mechanism, characteristic of polaron carriers and facilitated by the variable valences of iron as described by Eq. (5). Activation energies for conduction (E_σ) were found to be 0.23 and 0.25 eV for the $x=0.05$, 0.10 compositions, respectively. As tabulated in Table 4, the difference $E_\sigma - E_\alpha$ of $\sim$0.18, 0.22 eV, respectively, is consistent with other oxide systems [41,53,55] as well as the $x=0$ samples.

Eq. (8) was applied to the Seebeck coefficient data for the $x=0.05$ and 0.10 compositions to estimate carrier concentration for use in conjunction with electrical conductivity values in the determination of the mobility. The zinc dopant served to increase carrier concentration in the $x=0.05$, 0.10 ($\sim 2\times10^{21}$, $\sim 4\times10^{21}$ cm^{-3}, respectively) samples by almost an order of magnitude as compared to undoped samples ($\sim 2\times10^{20}$ cm^{-3}). While hole concentration remained fairly constant with temperature in the doped compositions, the mobility evolved from $\sim 6\times10^{-5}$ cm^2/Vs at 100 °C to a maximum of 0.005 cm^2/Vs at 800 °C. The magnitude of these values, at <0.01 cm^2/Vs, provides further support of a polaron conduction mechanism.

5. Conclusion

The thermoelectric properties of Zn-doped dicalcium ferrite exhibited *p*-type conduction, with transport analyses revealing a polaron conduction mechanism. The presence of zinc dopant served to increase electrical conductivity to a maximum of $\sim$3.4 S/cm, and decrease thermal conductivity to 1.5 W/mK, while maintaining a Seebeck coefficient >100 μV/K. While these values are competitive in terms of brownmillerite polycrystalline ceramics, the low power factor restricts the figure of merit values to <1.

Two new phase transitions were discovered in $Ca_2Fe_2O_5$ at temperatures above 900 °C; the first from incommensurate to commensurate, and the second to statistically disordered chain sequence represented by space group *Imma*. Zn doping decreased the onset temperatures of both the Néel transition and the *Pnma–Imma*(0 0 γ)*s*00 phase transition temperatures. Notably, the presence of Zn results in a transition to a *commensurately* modulated high temperature phase rather than an incommensurately modulated one. Both a decrease in the rate of *Pnma–Imma*(0 0 γ)*s*00 transformation and lower onset temperatures for the reverse transformation were observed with increasing dopant, illustrating a thermal hysteresis in the phase transition that increased with zinc concentration. These direct relationships between zinc dopant and the high-temperature phase behavior are attributed to its tetrahedral occupancy and the central role of tetrahedra in the phase transition. This ability to target acceptor ions at specified sites in the brownmillerite structure and directly control the high-temperature phase behavior may present new opportunities for designing brownmillerite compounds for high-temperature applications.

Acknowledgments

The authors acknowledge Swavek Zdzieszynski for his assistance with high temperature X-ray diffraction facilities, and Soory Kabbekodu at ICDD for help with modulated structures. E.A.-S. gratefully acknowledges support from the National Science Foundation Graduate Research Fellowship Program.

References

[1] A.L. Shaula, Y.V. Pivak, J.C. Waerenborgh, P. Gaczyñski, A.A. Yaremchenko, V.V. Kharton, Solid State Ionics 177 (33–34) (2006) 2923–2930.
[2] N. Sharma, K.M. Shaju, G.V.S. Rao, B.V.R. Chowdari, Electrochim. Acta 49 (7) (2004) 1035–1043.
[3] Y. Yang, Z. Cao, Y. Jiang, L. Liu, Y. Sun, Mater. Sci. Eng. B 132 (3) (2006) 311–314.
[4] A. Kawashima, K. Matsubara, K. Honda, Bioresour. Technol. 99 (9) (2008) 3439–3443.
[5] D. Hirabayashi, T. Yoshikawa, K. Mochizuki, K. Suzuki, Y. Sakai, Catal. Lett. 110 (3–4) (2006) 269–274.
[6] M.T. Anderson, J.T. Vaughey, K.R. Poeppelmeier, Chem. Mater. 5 (2) (1993) 151–165.
[7] G.B. Zhang, D.M. Smyth, Solid State Ionics 82 (3–4) (1995) 161–172.
[8] T.G. Parsons, H. D'Hondt, J. Hadermann, M.A. Hayward, Chem. Mater. 21 (2009) 5527–5538.
[9] H. D'Hondt, A.M. Abakumov, J. Hadermann, A.S. Kalyuzhnaya, M.G. Rozova, E.V. Antipov, G. vanTendeloo, Chem. Mater. 20 (2008) 7188–7194.
[10] G.J. Redhammer, G. Tippelt, G. Roth, R.G. Amthauer, Am. Mineral. 89 (2–3) (2004) 405–420.
[11] H. Krüger, V. Kahlenberg, V. Petříček, F. Phillipp, W. Wertl, J. Solid State Chem. 182 (6) (2009) 1515–1523.
[12] S.A. Speakman, J.W. Richardson, B.J. Mitchell, S.T. Misture, Solid State Ionics 149 (2002) 247–259.
[13] C.B. Vanpeteghem, R.J. Angel, J. Zhao, N.L. Ross, G.J. Redhammer, F. Seifert, Phys. Chem. Minerals 35 (9) (2008) 493–504.
[14] P. Berastegui, S.-G. Eriksson, S. Hull, Mater. Res. Bull. 34 (2) (1999) 303–314.
[15] R.J.D. Tilley, Defects in Solids, John Wiley & Sons, Hoboken, NJ, 2008.
[16] E. Asenath-Smith, I.N. Lokuhewa, S.T. Misture, D.D. Edwards, J. Solid State Chem. 183 (2010) 1670–1677.
[17] M.V. Patrakeev, I.A. Leonidov, V.L. Kozhevnikov, K.R. Poeppelmeier, J. Solid State Chem. 178 (3) (2005) 921–927.
[18] H.D. Zhou, J.B. Goodenough, J. Solid State Chem. 178 (12) (2005) 3679–3685.
[19] K. Kobayashi, S. Yamaguchi, T. Tsunoda, Y. Imai, Solid State Ionics 144 (1–2) (2001) 123–132.
[20] J.C. Waerenborgh, D.P. Rojas, N.P. Vyshatko, A.L. Shaula, V.V. Kharton, I.P. Marozau, E.N. Naumovich, Mater. Lett. 57 (2003) 4388–4393.
[21] R. Benloucif, N. Nguyen, J.M. Genenche, R. Raveau, J. Phys. Chem. Solids 51 (1) (1990) 79–83.
[22] C.D.L. Calle, J.A. Alonso, A. Aguader, M.T. Fernández-Díaz, Dalton Trans. 21 (2009) 4104–4114.
[23] J.D. Dunitz, L.E. Orgel, J. Phys. Chem. Solids 3 (1957) 20–29.
[24] J.D. Dunitz, L.E. Orgel, J. Phys. Chem. Solids 3 (1957) 318–323.
[25] A.P. Grosvenor, J.E. Greedan, J. Phys. Chem. C 113 (2009) 11366–11372.
[26] I. Matsubara, R. Funahashi, T. Takeuchi, S. Sodeoka, T. Shimizu, K. Ueno, Appl. Phys. Lett. 78 (23) (2001) 3627–3629.
[27] A. Kosuga, S. Urata, K. Kurosaki, S. Yamanaka, R. Funahashi, Jpn. J. Appl. Phys. 47 (8) (2008) 6399–6403.
[28] D.D. Pollock, Thermoelectricity: Theory, Thermometry, Tool, American Society for Testing and Materials, Philadelphia, PA, 1985, pp. 111–132.
[29] S.T. Misture, Meas. Sci. Technol. 14 (2003) 1091–1098.
[30] V. Petříček, M. Dušek, L. Palatinus, JANA2006, Institute of Physics, Praha, Czech Republic, 2006.
[31] A. Trestman-Matts, S.E. Dorris, T.O. Mason, J. Am. Ceram. Soc. 66 (8) (1983) 589–592.
[32] F. Kanamaru, H. Miyamoto, Y. Mimura, M. Koizumi, M. Shimada, S. Kume, S. Shin, Mater. Res. Bull. 5 (1970) 257–262.
[33] Y. Iwamoto, T. Ebihara, N. Harrison, M. Jaime, A. Silhanek, K. Tezuka, K. Morishita, T. Terashima, A. Iyo, J. Magn. Magn. Mater. 310 (2) (2007) 300–302.
[34] A.M. Abakumov, A.M. Alekseeva, M.G. Rozova, E.V. Antipov, O.I. Lebedev, G.V. Tendeloo, J. Solid State Chem. 174 (2003) 319–328.
[35] A.M. Abakumov, A.S. Kalyuzhnaya, M.G. Rozova, E.V. Antipov, J. Hadermann, G.v. Tendeloo, Solid State Sci. 7 (2005) 801–811.
[36] K. Fukuda, H. Ando, J. Am. Ceram. Soc. 85 (5) (2002) 1300–1302.
[37] H. Krüger, V. Kahlenberg, Acta Crystallogr. Sect. B: Struct. Sci. B61 (2005) 656–662.
[38] P.A. Cox, Transition Metal Oxides: An Introduction to Their Electronic Structure and Properties, Clarendon Press, Oxford, 1995.
[39] N.F. Mott, Metal–Insulator Transitions, Taylor & Francis, London, 1974.
[40] R.W. Rice, Porosity of Ceramics, Marcel Dekker, New York, 1998, p. 44.
[41] W. Kobayashi, A. Satake, I. Terasaki, Jpn. J. Appl. Phys. 41 (1) (2002) 3025–3028.
[42] C. Picard, P. Gerdanian, Solid State Commun. 87 (9) (1993) 775–778.
[43] A.N. Lavrov, L.P. Kozeeva, Physica C (Amsterdam) 248 (1995) 365–381.
[44] T.E. Whall, N. Salerno, Y.G. Proykova, V.A.M. Brabers, Philos. Mag. B 56 (1) (1987) 99–105.
[45] D.V. Ragone, in: C. Robichaud (Ed.), Thermodynamics of Materials, vol. II, John Wiley & Sons, Inc., United States, 1995, pp. 221–238.
[46] L. Onsager, Phys. Rev. 38 (1931) 2265–2279.
[47] L. Onsager, Phys. Rev. 37 (4) (1931) 405–426.
[48] I. Terasaki Chapter 10 Introduction to Thermoelectricity. 〈http://www.f.waseda.jp/terra/pdf/thermoelectricity.pdf〉 (December 1, 2008).
[49] K. Koumoto, I. Terasaki, R. Funahashi, MRS Bull. 31 (3) (2006) 206–210.

[50] U. Wang, N.S. Rogado, R.J. Cava, N.P. Ong, Nature 423 (2003) 425–428.
[51] J.-P. Doumerc, J. Solid State Chem. 109 (1994) 419–420.
[52] P.M. Chaikin, in: V.Z. Kresin, W.A. Little (Eds.), Organic Superconductivity, Plenum Press, New York, 1990, pp. 101–115.
[53] H.L. Tuller, A.S. Nowick, J. Phys. Chem. Solids 38 (8) (1977) 859–867.
[54] N.F. Mott, E.A. Davis, Electronic Processes in Non-crystalline Materials, Clarendon Press, Oxford, 1979.
[55] T.O. Mason, H.K. Bowen, J. Am. Ceram. Soc. 64 (4) (1981) 237–242.
[56] A.J. Wright, H.M. Palmer, P.A. Anderson, C. Greaves, J. Mater. Chem. 12 (2002) 978–982.